RMetS
Royal Meteorological Society

A radius–depth model for midlatitude cyclones in reanalysis data and simulations

Andrea Schneidereit, Richard Blender and Klaus Fraedrich*
Meteorologisches Institut, Universität Hamburg, KlimaCampus, Grindelberg 5, D-20144 Hamburg, Germany
*Correspondence to: Klaus Fraedrich, Meteorologisches Institut, Universität Hamburg, Grindelberg 5, D-20144 Hamburg, Germany. E-mail: klaus.fraedrich@zmaw.de

Geometric properties of winter (DJF) and summer (JJA) midlatitude cyclones are analysed in reanalysis data, present-day and global warming simulations. Cyclone centres are identified by the minima of the 1000 hPa geopotential height. Fitting an azimuthally symmetric Gaussian function to the surrounding height field provides cyclone depth (difference between the cyclone centre and the synoptic environment), radius (standard deviation), geostrophic wind and vorticity. Analysing ERA-40 reanalysis data of different resolutions and Intergovernmental Panel on Climate Change (IPCC) scenario simulations by the coupled atmosphere–ocean general circulation model ECHAM5/MPI-OM yields mean radii of 300–500 km in winter and 300–400 km in summer. Depth maxima occur in the storm tracks (determined by the bandpass-filtered variance of the geopotential height), and the smallest radii characterize oceanic cyclogenesis regions. The geostrophic vorticity, derived from the fitted Gaussian model, agrees reasonably well with the observed relative vorticity. Future warmer climate scenarios exhibit smaller radii and weaker depths during winter and summer. An intense growth of the depth is found during the 2–10 day cyclone life cycles, while the radii reveal negligible growth. Compositing depths with respect to normalized total lifetime leads to rescaled depth life cycles, which collapse to a simple universal function, $\tilde{a}(1-\tilde{a})$, for relative cyclone age $\tilde{a}$. Copyright © 2010 Royal Meteorological Society

Key Words: cyclone radius; climate change; life cycles

Received 13 May 2009; Revised 27 August 2009; Accepted 27 August 2009; Published online in Wiley InterScience 19 January 2010

Citation: Schneidereit A, Blender R, Fraedrich K. 2010. A radius–depth model for midlatitude cyclones in reanalysis data and simulations. *Q. J. R. Meteorol. Soc.* **136**: 50–60. DOI:10.1002/qj.523

1. Introduction

Weather and climate in the midlatitudes are determined by low-pressure systems, which are the source of precipitation and storms. To foster an understanding of the complex geometric structure of cyclones, two-dimensional approaches characterizing the main geometric properties of the depressions in terms of radius and depth have been suggested. Previous methods of radius determination can be summarized as based on (1) the derivative of the pressure, (2) the enclosed area or (3) a functional fit. The cyclone depths are calculated in a further step considering pressure information in the vicinity of a cyclone centre.

Nielsen and Dole (1992) were the first to derive horizontal size distributions of synoptic cyclones by analysing North Pacific low-pressure systems in surface analyses. The authors point out four methods to determine a cyclone radius: the distance to (1) the nearest high-pressure centre, (2) the nearest cyclone centre, (3) the nearest saddle point, and (4) the area enclosed by the largest closed isobar. Only the two last methods (3, 4) yield meaningful results. Nielsen and Dole concentrate on definition (3), analysing the largest scales reached during the cyclone lifetime, denoted as the maximum cyclone radius. The frequency distribution of the maximum radius is concentrated in the range 300–600 km but reaches 1500 km in rare cases. A main result is that the scale of the majority of cyclones is subsynoptic, i.e. lower than predicted by baroclinic instability theory. The concept of the largest closed isobar is used by Wernli and Schwierz (2006), who detect a mean growth of the radius from 350 km to 800 km at the fourth day. Rudeva and Gulev (2007) and Rudeva (2008) determine effective radii by searching local extrema along radial lines. This method is also able to define the asymmetry of cyclones. The authors find a cyclonic growth of 50% to 150% during the development stage.

Patoux *et al.* (2009) analyse the radii and depths of southern hemispheric cyclones during 1999–2006 in European Centre for Medium-Range Weather Forecasts (ECMWF) analyses, which are corrected by a wavelet analysis of satellite data. The cyclone tracking is based on the method developed by Murray and Simmonds (1991). The radii are determined at distances where the pressure gradient decreases below a subjective threshold, and range from 400–1000 km. The depths are given by the corresponding pressure deviations from the centre.

Grotjahn *et al.* (1999) focus on the evolution of the size of synoptic cyclones and apply a wavelet transform analysis (Mexican hat) to longitudinal and latitudinal cross-sections of sea-level pressure data. The analysis, restricted to 12 cyclones, shows that the radius, given by the average of longitudinal and latitudinal wavelet scales, doubles at four days during the life cycle. The main advantage of applying wavelet analysis is that the pressure field in a synoptic neighbourhood is included. Therefore, the method provides a joint estimation of both radius and depth.

Grotjahn and Castello (2000) introduce an alternative approach identifying the size of extratropical cyclones based on the circular average of the geostrophic kinetic energy. The maxima of the kinetic energy are within 450–650 km and the radii, which are determined by comparison with a threshold level, reach 1200 km.

Simmonds and Keay (2000) determine the radius R and the depth D of a cyclone through a relationship between depth, radius and the Laplacian of the pressure in the cyclone centre:

$$D = \frac{1}{4} R^2 \nabla^2 p. \tag{1}$$

The radius can be determined either by an area of positive Laplacian (or positive vorticity if the geostrophic approximation is presumed) or by considering saddle points along radial lines emanating from the cyclone centre (Lim and Simmonds, 2007). Simmonds (2000) finds an increase of the radii of 33% over the first four days. These results are in qualitative agreement with the findings of Grotjahn *et al.* (1999).

Trigo *et al.* (1999) determine the radii of Mediterranean cyclones from the distance between the centre and the outermost closed isobar (as in Nielsen and Dole, 1992). The authors find that the majority of cyclones have radii in range 300–550 km, with an average below 500 km. Therefore, the detected cyclones are located at the mesoscale and subsynoptic scale.

A filtering method is suggested by Benestad and Chen (2006) who transform the sea-level pressure (SLP) data to a truncated Fourier series for the latitudinal and longitudinal profiles; these provide analytical expressions for cyclone centres and radii. The radii could be determined as the minimum distance between the cyclone centre and the points of inflection in the latitudinal and longitudinal directions.

The aim of this analysis is to estimate the geometric structure of midlatitude cyclones from a combination of radius and depth. The method is based on an optimal fit of a Gaussian function to the radially dependent geopotential height field in the neighbourhood of the geopotential height minimum. The approach is tested for different grid resolutions and applied to reanalysed and simulated data. The time evolution of both radius and depth provides information on the cyclone life cycle. This integral approach avoids a number of problems caused by deviations from azimuthal symmetry and the finite resolution of gridded data.

Section 2 presents the observational and simulated data and the cyclone tracking. The Gaussian model for radius and depth is introduced in section 3. The climatologies of cyclone density, radius and depth obtained from reanalysis, a present-day simulation and a warmer climate scenario are presented in section 4. The analysed life cycles of radius and depth in the reanalysis data are shown in section 5. A summary and discussion is given in section 6.

2. Data and cyclone tracking

The cyclones are analysed and tracked in the geopotential height fields of the reanalysis of the European Centre for Medium-Range Weather Forecasts (ECMWF) and in coupled atmosphere–ocean model simulations with ECHAM5/MPI-OM.

2.1. Data

The 45 year reanalysis data set ERA-40 of the ECMWF covers the period from September 1957–August 2002 (Uppala *et al.*, 2005). The model resolution is the spectral triangular truncation $T159$ with 60 vertical model levels (see Simmons, 2001, including a description of the data assimilation system). Changes in the observing system in 1979 led to artificial trends, which are most pronounced in the Southern Hemisphere (Bengtsson *et al.*, 2006). To determine the impact of the resolution on the cyclone geometry, the ERA-40 data are analysed in grid data corresponding to $T106$, $T63$ and $T42$ spectral resolution with a six-hour time step. Note that the model data are given with $T63$ resolution (see below).

The simulated data are based on Intergovernmental Panel on Climate Change (IPCC) scenario simulations (Nakicenovic *et al.*, 2000) performed by the coupled atmospheric–ocean general circulation model (GCM) ECHAM5/MPI-OM (Marsland *et al.*, 2003; Roeckner *et al.*, 2003). The atmosphere is simulated with spectral resolution $T63$ and 31 vertical model levels, while the oceanic fields have approximately a 1.5° resolution over 40 vertical levels. The coupling is implemented without flux corrections (Jungclaus *et al.*, 2006). The temporal resolution is 6 h as in the reanalysis.

For the comparison with the ERA-40 data a present-day climate simulation is analysed; a warm climate simulation, based on a scenario with a moderate increase of greenhouse gases, complements this analysis. The twentieth century (hereafter 20C) is simulated with observed greenhouse gas concentrations, aerosols and solar and volcanic forcings. Three ensemble members are available, initialized from a control simulation. For an overlap with the reanalysis period, the analysis is restricted to 1950–2000.

The warmer climate is based on an ensemble simulation according to the moderate A1B scenario (see Nakicenovic *et al.*, 2000, for details), with a doubling of the CO_2 concentration from 2000 to 2100. This scenario is augmented by a simulation for 2100–2200 with greenhouse gas concentration fixed at the 2100 level (stabilization run). Since this simulation does not reach stationarity in the first part of the run, the present study concentrates on the period from 2150–2200.

2.2. *Cyclone tracking*

Different approaches for the tracks of cyclones have been developed by, for example, Murray and Simmonds (1991), König *et al.* (1993), Hodges (1994), Sinclair (1994) and Grigoriev *et al.* (2000); for a recent review see Ulbrich *et al.* (2009). In this study the cyclone identification and tracking of Blender *et al.* (1997; see also Sickmöller *et al.*, 2000) is used. The lows are defined by mimima of the geopotential height with a minimum gradient of 50 gpm 1000km^{-1} (where gpm denotes geopotential metres). The cyclone tracks are determined by connecting nearby cyclones at subsequent time steps with a maximum distance (speed) condition. To avoid spurious detections, a minimum lifetime of 2 days (at least nine subsequent 6 h time steps) is required. Note that the number of cyclones decreases to roughly 60% if the minimum lifetime is increased by one day.

The cyclones are tracked in the Northern Hemisphere (30°–90°N) beside regions with orography above 500 m. The Himalayas and adjacent regions (50°–110°E, south of 35°N) are excluded to neglect summer heat lows and monsoon-induced depressions. A cyclone density is defined by the number of occurrences normalized by the number of observations and by the sampling area of 10^6 km^2. These densities are determined for the individual winters (DJF) and summers (JJA) to derive interannual variabilities.

3. Cyclone geometry

In this section the Gaussian radius–depth is introduced and validated using geostrophic data. The geopotential height $z = \Phi/g$ of the 1000 hPa geopotential surface Φ is approximated by a Gaussian in the neighbourhood of the minima. Thus, the function assumes azimuthal symmetry for the whole life cycle to avoid problems that may occur if different directions are analysed separately with subsequent averaging. For open depressions, which are included if the averaged geopotential height gradient exceeds a given threshold, the radius can be considered as a characteristic horizontal extension. The Gaussian function is fitted by a least-squares method; it is written as

$$z_G(r) = z_{env} - D\exp(-r^2/2R^2), \tag{2}$$

where z_{env} is the mean of the geopotential height in the environment, a region well outside the central region. The two fitted parameters are the radius R and the environment z_{env}. The radius R is the standard deviation of the Gaussian function, which is located at the point of maximum derivative (point of inflection). Note that the depth D is not fitted but determined by the difference between the environment z_{env} and the known central geopotential height value $z_G(r = 0)$. The optimization for the environmental value of the geopotential height z_{env} is initialized by the mean of the geopotential height in a larger region (about 1000×1000 km^2) and the radius R is initialized by 500 km. Figure 1(a) shows the fit of the Gaussian model to the geopotential height values in the vicinity of a selected cyclone centre (63°W, 59°N) on 3 December 1957 at 0000 UTC. Grid points used for the optimization are indicated by dark grey coloured points. The optimization is successful (this means a convergence criterion is attained) for distinctly more than 99% of cyclones. The remaining cyclones are ignored in the analysis.

In Figure 1(b) the behaviour of the function z_G is displayed for vanishing z_{env} and constant radius $R = 500$ km. Thus the radius R, as defined here, shows notably smaller values than those radii that might be obtained by considering the far neighbourhood, for example the nearest saddle points or outermost closed isobars (hereafter R_{env}). For a comparison with the Gaussian model, definitions for R_{env} can be considered as given by intersections of constant geopotential height z with the Gaussian. The magnitude of R can be estimated as roughly one half of R_{env}. While the radius in the present publication can be scaled somehow to the radius found in other analyses, an important difference remains: R_{env} grows for increasing depth D if the radius R remains constant. This explains the major deviations obtained by the Gaussian model compared with other radius definitions.

The present method is related to the wavelet analysis of Grotjahn *et al.* (1999), with the main difference that this approach starts from azimuthal symmetry (perhaps this is the reason that numerical problems can be avoided). Mathematically there is some correspondence, since the Gaussian and the Mexican hat wavelet can both be considered as Hermite polynomials multiplied by an exponential decay: while the Gaussian is the zeroth polynomial, the Mexican hat wavelet has the shape of the first Hermite polynomial. Probably due to the averaging, the present method can be applied to climatologically relevant numbers of cyclones without numerical obstacles.

3.1. *Geostrophic wind and vorticity in the Gaussian model*

The Gaussian function for the geopotential height $z_G(r)$ yields geostrophically approximated wind and vorticity fields. The components of the geostrophic wind are

$$u_g = -\frac{g}{f}\frac{\partial z}{\partial y}, \qquad v_g = \frac{g}{f}\frac{\partial z}{\partial x}, \tag{3}$$

with the Coriolis parameter $f = 2\Omega\cos\phi$. Due to the definition of the radius (point of inflection of the Gaussian function), the maximum geostrophic wind is located at the radius. To corroborate this, the geostrophic wind is calculated according to (3) for a specific date. Figure 2 shows the geostrophic and observed wind at 1000 hPa on 1 December 1957 at 0000 UTC. The black circles indicate the radii for the seven detected extratropical cyclones. The geostrophic wind maxima are located at the radii (Figure 2(a)). The observed wind maxima, which are distinctly lower compared with the geostrophic wind, are well situated at the radius R (Figure 2(b)).

According to the Gaussian model, the maximum kinetic energy is located at the radius. Furthermore, the total

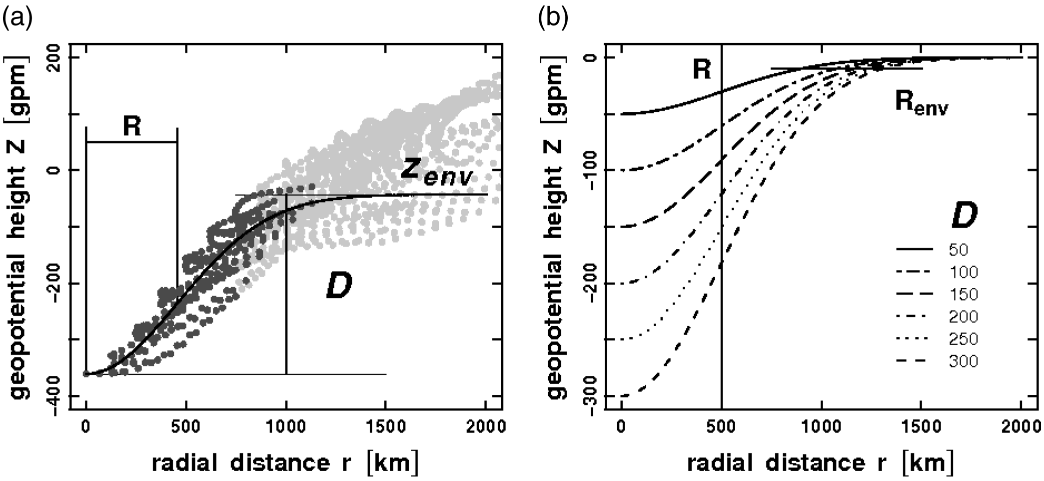

Figure 1. (a) Gaussian model fitted to geopotential height data in the vicinity of a low-pressure centre with radius R and depth D. The bold data are used for fitting. (b) Gaussian model for the geopotential height z_G with different cyclone depths D and constant radii $R = 500$ km. The intersections indicate radii increasing with depth.

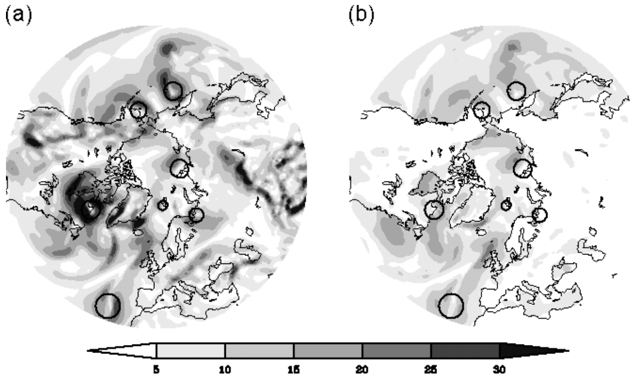

Figure 2. (a) Geostrophic wind at 1000 hPa calculated from ERA-40 data; (b) wind speed at 1000 hPa obtained ERA-40 data; circles in both panels indicate the radius determined.

kinetic energy in a pressure level is proportional to D^2, but independent of the radius.

The geostrophic vorticity in the cyclone centre ($r = 0$) is defined by radius and depth (see (2)) as

$$\zeta_G = \frac{g}{f}\nabla^2 z_G(r) = \frac{g}{f}\frac{D}{R^2}. \tag{4}$$

The vorticity ζ_G agrees well with the geostrophic vorticity ζ_{g1000}, determined by the Laplacian of the geopotential height at 1000 hPa (see Figure 3(a)). This figure includes all winter cyclones detected for the ERA-40 period.

A more stringent test of the approximation is given by comparing the approximated vorticity ζ_G at 1000 hPa with the relative vorticity at 850 hPa, hereafter ζ_{850} (see Figure 3(b)). Instead of 1000 hPa, the 850 hPa level is selected, because the lower level is influenced by surface friction, which leads to higher deviations from geostrophic balance. This comparison reveals pronounced discrepancies, which are visible as deviations from a linear correlation.

3.2. *Resolution dependence of the geometric properties*

The dependence of the geometric properties on the spatial resolution of the geopotential height data is determined by comparing their radii and depths at three different resolutions $T42$, $T63$ and $T106$. The numbers of cyclones decreases with coarser resolution (Blender and Schubert, 2000) and cyclonic characteristics (lifetime, maximum deepening rate, etc.) depend on the grid used (Jung *et al.*, 2006); this affects shallow cyclones in particular.

The frequency distributions for radii in winter and summer (Figure 4(a) and (b)) reveal similar characteristics for different resolutions. For coarser resolutions the distributions shift to higher radii. In the $T42$ case, cyclones with radii less than 200 km are nearly absent, whereas cyclones with radii greater than 400 km dominate the distribution.

Figure 4(c) and (d) shows the frequency distributions of the depths for winter and summer, respectively. The behaviour of the depth, which itself is dependent on the resolution, shows that the coarser the resolution the lower the number of small depths (below 100 gpm). For decreasing resolution, the number of detected cyclones with depths above 400 gpm increases. In summer there is no definite behaviour detectable for intense cyclones.

In summary, the number of large values of radii and depths increases for coarser resolution, independent of the season considered.

4. Climatologies

The following section presents the climatologies of cyclone densities (occurrences) and radii and depths for ERA-40 data and simulations with ECHAM5/MPI-OM. Both data sets are considered for the same spatial resolution ($T63$). The cyclone densities of the simulations are presented as ensemble means (three members).

4.1. *Cyclone densities*

The cyclone density in the ERA-40 reanalysis (Figure 5(a) and (b)) shows the cyclone tracks with largest values over the northern parts of the North Atlantic and North Pacific. During winter, maxima are further north and more intense than in summer. The Mediterranean shows a further maximum of the cyclone density during winter.

The climatology of the cyclone density in the ECHAM5/MPI-OM present-day simulation (20C) corresponds well to the ERA-40 reanalysis (Figure 5(a)–(d)).

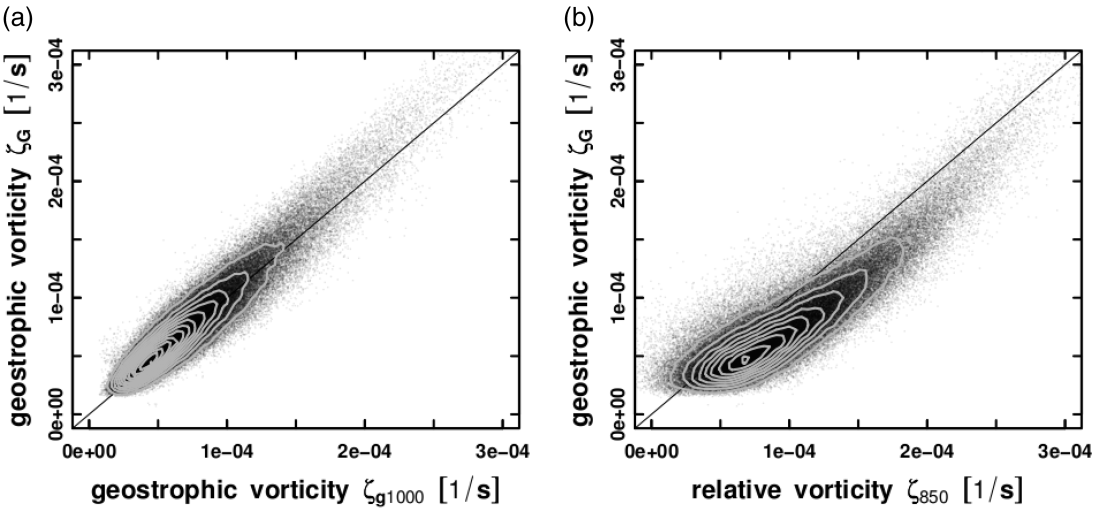

Figure 3. Scatter diagram and density of the vorticity ζ_{Gauss} derived from the Gaussian model (4) versus (a) geostrophically approximated vorticity ζ_g at 1000 hPa and (b) relative vorticity at 850 hPa in the cyclone centre for winter. The solid line denotes perfect correlation.

However, the 20C simulation shows deviations from ERA-40 in the spatial extension and the magnitude of the cyclone density, which are both most pronounced over the North Pacific (winter and summer), the North Atlantic and, less strongly, in the Mediterranean. In summer, ERA-40 shows a distinct maximum southeast of the Black Sea (Figure 5(b)), which may be due to the semi-permanent extension of the Indian monsoon (see Trigo *et al.*, 1999). In the present-day simulation this maximum is much weaker, possibly a consequence of the deficiency of the model to produce variability in the high wave number domain. These deviations are probably due to the model design, for example with regard to orography and ice cover (Bengtsson *et al.*, 2006). However, the cyclone densities of the model correspond to ERA-40, especially for winter (Löptien *et al.*, 2008). The 20C scenario agrees reasonably well with the NCEP/NCAR reanalysis data despite some discrepancies in magnitude and the location of the maxima (Pinto *et al.*, 2007). Note that the cyclone density is only a measure of the number of cyclones per grid point without any information about their intensity.

In the warmer climate simulation (A1B) the total number of detected cyclones of the coupled model ECHAM5/MPI-OM shows no increase compared with the twentieth century simulation. In winter, the Pacific maximum of the cyclone density reveals a northeastward shift compared with the present-day simulation (Figure 5(e)–(f)), whereas the poleward shift of the Atlantic maximum is less pronounced. In the North Atlantic, the poleward shift is accompanied by enhanced numbers of cyclones at the east coast of North America and north of the British Isles (see Bengtsson *et al.*, 2006, for a similar analysis with a different tracking scheme). Note that the increase in cyclone density in this area is more pronounced in the 21st century than during the stabilization run in 2100–2200 (not shown). The subtropics show a decreasing cyclone density in winter. This reduction is distinct in the Mediterranean, a result that is also found by Bengtsson *et al.* (2006), Pinto *et al.* (2007) and Löptien *et al.* (2008). In summer, the North Atlantic cyclone density shows a northward shift, whereas in the North Pacific a southward displacement is obvious (Figure 5(f)). Over the Mediterranean and the adjacent western and eastern coast, the cyclone density increases.

It is noteworthy that the cyclone density changes are much less pronounced in the A1B scenario than in scenario simulations according to the A2 and previous model version ECHAM3/LSG (Schubert *et al.*, 1998), indicating the dependence of changes in cyclone density on the greenhouse gas forcing (Pinto *et al.*, 2009) and on model versions.

4.2. *Radius and depth in ERA-40 data*

The northern hemispheric distributions of radius and depth for winter and summer of the ERA-40 time period are shown in Figure 6. All depressions detected during the cyclone life cycles are included in the figures. Note that the reanalysis data are analysed with the same spectral resolution ($T63$) as the model.

The frequencies of the cyclone radii in the climatological mean show a broad distribution, with the highest numbers in the range 300–500 km; the largest radii reach 1000 km (Figure 6(a)). During winter the cyclones are distinctly larger in comparison with summer. The frequency distribution of the depths reveals weaker and more shallow summer cyclones (Figure 6(b)).

The geographical distributions of the mean cyclone radii show a seasonal cycle, with higher means attained during winter (Figure 7(a) and (b); compare this with Figure 6(b)). These mean radius maps are determined at grid points with at least 10 cyclone counts during the whole time period. The mean radii are smallest in the oceanic genesis regions of the Northern Hemispheric cyclone tracks (about 300–375 km). This pertains also to cyclones detected in the lee of Rocky Mountains (note that regions with orography above 500 m are excluded in the cyclone detection). Cyclones with large radii are located southeast of the two storm tracks (determined by the bandpass-filtered variance of the geopotential height) and in the North Pacific near the Aleutian Islands during winter. In summer the spatial pattern shows similar characteristics to the winter pattern, however with consistently smaller values (compare the frequency distribution in Figure 6a). The geographical distributions of the radii do not represent the storm tracks.

Simmonds (2000) and Rudeva and Gulev (2007) find that during the genesis the mean radii range from 300–500 km, and that the radii increase distinctly during intensification.

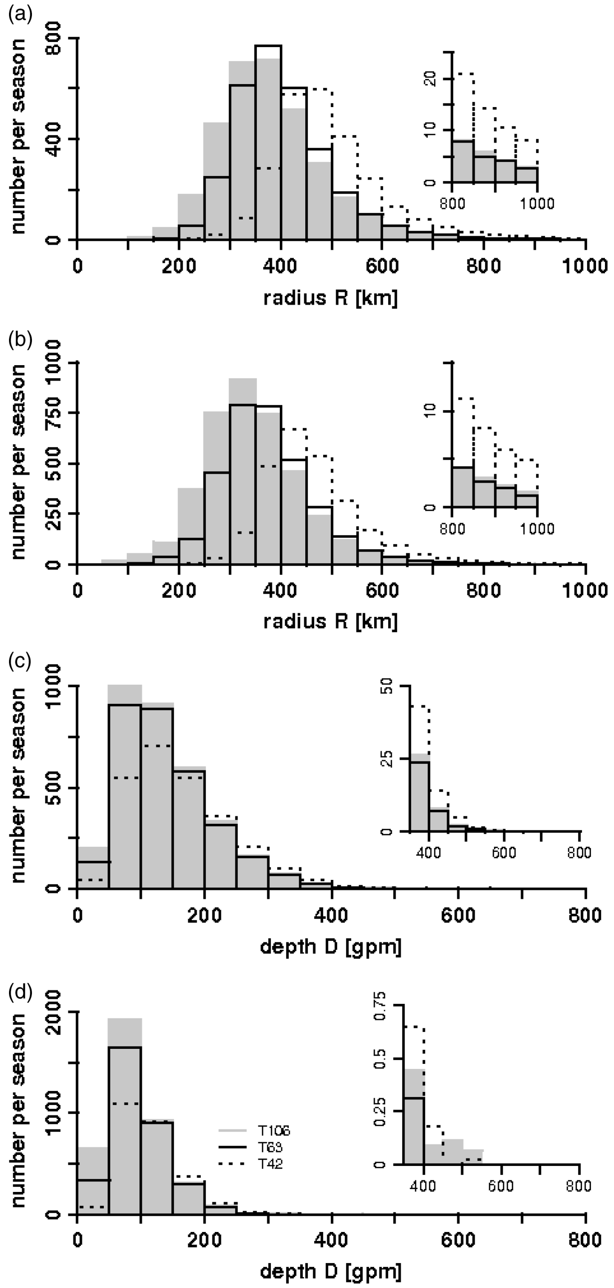

Figure 4. Frequency distributions of radii for (a) winter (DJF) and (b) summer (JJA), and depths for (c) winter (DJF) and (d) summer (JJA) in ERA-40 reanalysis data with different resolutions. The insets show the corresponding behaviour for high values of radius and depth.

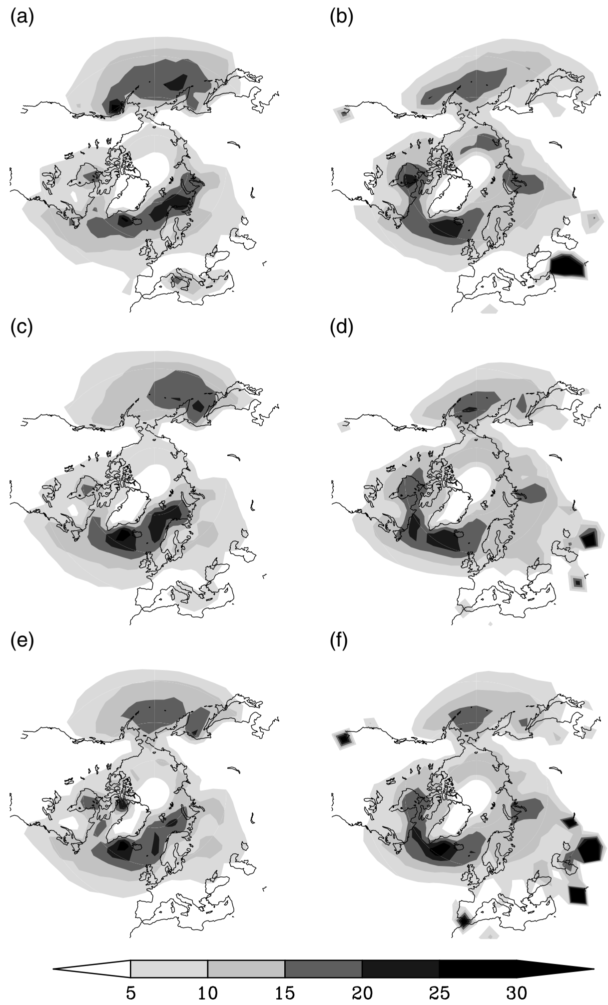

Figure 5. Cyclone densities of (a,b) ERA-40, (c,d) a present-day simulation according to 20C and (e,f) a warmer climate A1B scenario, for winter (left) and summer (right).

Owing to different definitions these radius distributions show considerably lower values than obtained by the present method (see Section 3). The two Northern Hemispheric storm tracks are well represented by the climatological depths (Figure 7(c) and (d)). The largest depth values are found slightly north of the maximum bandpass-filtered variability. This agrees with the findings of Simmonds and Keay (2002) for the climatological mean depth in the NCEP/NCAR reanalysis.

4.3. *Radius and depth in a warmer climate scenario*

The comparison of the cyclone densities between the simulated present-day climate and the ERA-40 reanalysis reveal the reliability of the ECHAM5 model simulations. Despite some discrepancies between the simulation and reanalysis, the coupled model ECHAM5/MPI-OM is able to represent the main cyclone characteristics (Bengtsson *et al.*, 2006; Pinto *et al.*, 2007; Löptien *et al.*, 2008). The number of cyclones in the Northern Hemisphere in 20C agrees with ERA-40 in winter and summer, while in the warmer climate (A1B) the number of winter cyclones decrease by roughly 5% in both basins (Bengtsson *et al.*, 2006) and the number of summer cyclones increases by a similar amount. The change of cyclone sizes in a warmer climate is determined by Jiang and Perrie (2007), who analyse autumn cyclones in the North Atlantic along the east coast of North America for present-day and climate change scenarios. Based on the maximum wind speed, Jiang and Perrie conclude that the cyclones tend to broaden in the climate change scenario compared with the present-day simulation.

The seasonal mean frequencies of the cyclone radii in the reanalysis, the simulated present-day climate (20C) and the A1B scenario are shown in Figure 8(a) and (b). The frequency distributions are ensemble means. The cyclone radius frequency distributions of the 20C simulation correspond to the ERA-40 reanalysis (see Figure 8(a) and (b)) with slight discrepancies for large cyclones: while the radii of the 20C simulation exhibit much similarity to ERA-40 in winter, the summer distribution is concentrated at larger cyclonic radii (Figure 8(b)).

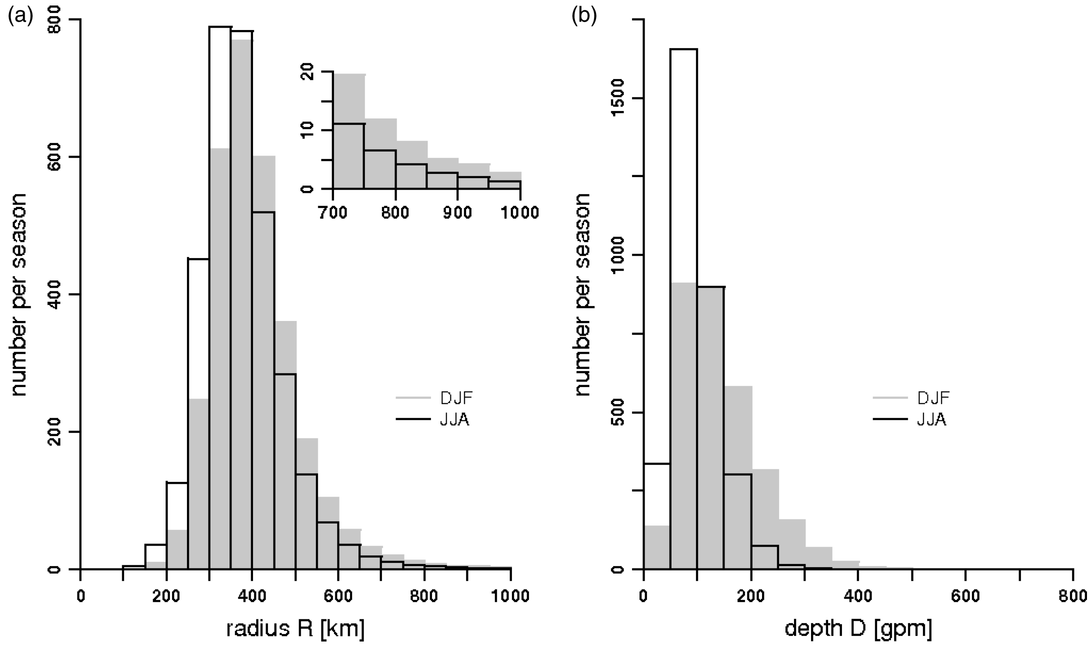

Figure 6. Frequency distributions of (a) radii and (b) depths for winter (grey-shaded) and summer (black-bordered) for ERA-40 reanalysis data. The inset shows the large-radius behaviour.

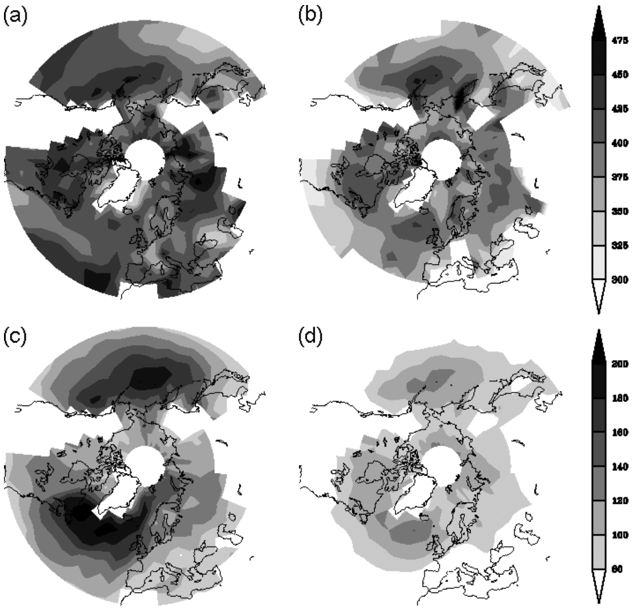

Figure 7. Spatial distribution of local means of (a,b) radii and (c,d) depths, for winter (left) and summer (right) in ERA-40 data.

The winter and summer frequency distributions of the cyclone depths are displayed in Figure 8(c) and (d) for the reanalysis, the present-day simulation and a warmer climate scenario. The winter as well as the summer frequency distributions of the cyclonic depth show an underestimation of small depths (up to 100 gpm) in 20C compared with the reanalysis. The distribution of high cyclonic depths agrees well in winter, whereas in summer the number is slightly overestimated in the present-day simulation.

In A1B, the number of cyclones with small radii (up to 400 km) decreases (Figure 8(a)) in winter while the number of large cyclones reveals a weak increase in a warmer climate compared with 20C. In summer the frequency distribution of the radii reveals a broadening, which is mainly due to an increase of the number of small radii. This is based on an increased number of cyclones over land, especially stationary cyclones.

The depths in a warmer climate during winter hint of a decrease in the number of weak cyclones compared with the present day. On the other hand, the number of intense cyclones increases. Thus, the distribution shows a broadening and a decrease of the most frequent intensities. In summer, the simulations predict more frequent weak cyclones. The most relevant aspect is the increase of intense cyclones in the Northern Hemisphere.

5. Life cycles of radius and depth

The majority of radius analyses find growth with maximum values up to twice the initial radius during the intensification phase. The maximum intensity attained during the life cycle of a cyclone depends on its total lifetime. According to Simmonds (2000) and Rudeva and Gulev (2007), the cyclones are combined in classes with identical total lifetimes (composites). In the 6 h data set the lifetimes are spread within the range of 2–10 days, hence classes are defined by 48, 54, 60, …, 240 h total lifetimes. Radii and depths in Figure 9 show distinct time evolution. The main results follow.

5.1. *Radius and depth*

The radii in winter show a weak life cycle with an initial mean of 390 km and a maximum mean of 460 km (Figure 9(a)). The variabilities of the mean radii in the classes are low. The total growth of the radii during the life cycles increases from 5% (2%) for the shortest to 40% (30%) for the longest total lifetime for winter (summer). In summer the growth rates are reduced and similar magnitudes are reached in classes with a longer lifetime. Note that the number of cyclones decreases with increasing total lifetime. This result deviates from previous analyses, which find a distinct growth of the

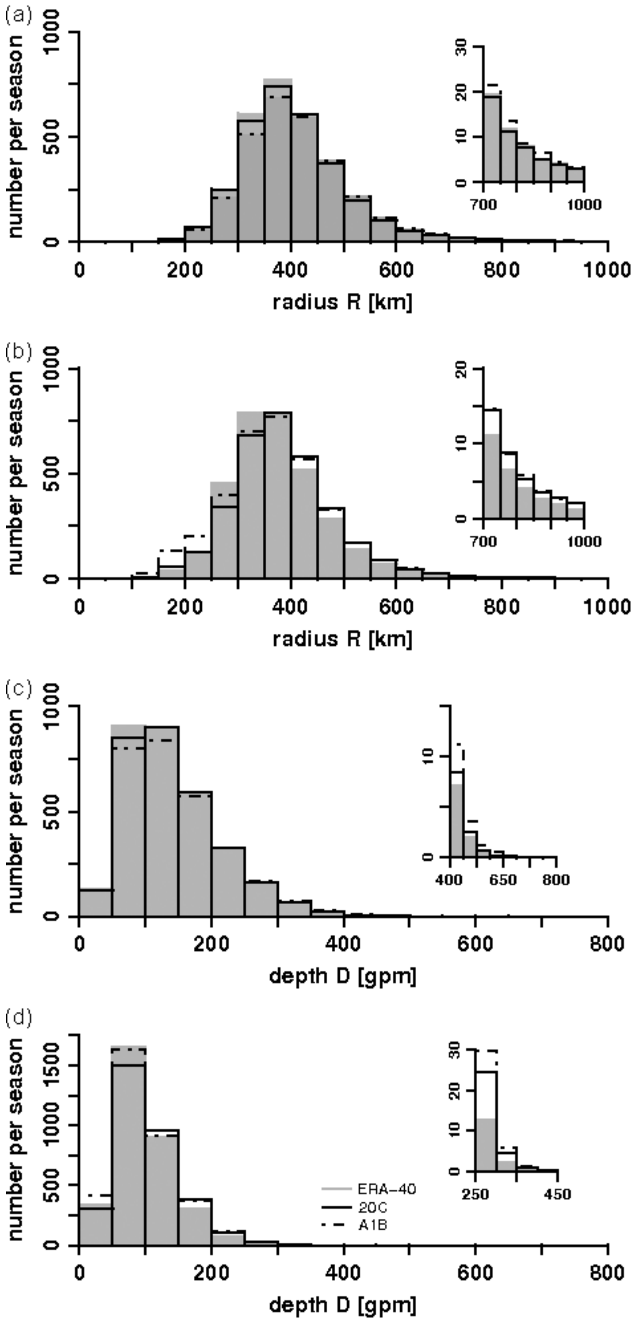

Figure 8. Warmer climate: frequency distributions of radii during (a) winter and (b) summer, and depth frequencies during (c) winter (DJF) and (d) summer (JJA) for ERA-40 (grey-filled), a present-day simulation according to 20C (solid) and a warmer climate according to A1B (dash–dotted). Large-value behaviour is shown in the insets.

radii. The different magnitudes of radii are easily explained by the different radius definitions (Section 3). Thus, during summer life cycles are almost absent in the radii, and the majority are within a narrow band in range 340–450 km (Figure 9(b)). The life cycles are terminated by a sudden decay.

The most remarkable life cycles are found for the depth during winter (Figure 9(c)). This result is comparable with the life cycle classes found by Rudeva and Gulev (2007) for the radii (compare Figure 1(b)). The total growth of the depth during the life cycles increases from 30% (20%) for the shortest living cyclones to about 150% (110%) for the longest-lived depressions for winter (summer). The initial growth does not depend on the class, i.e. the total lifetime. During summer the life cycles in the classes reveal less variability and much less growth, within 20–80 gpm compared with 40–160 gpm in winter. Here, there is also a relation between the growth in the mean depth and the total lifetime. In addition to the radius, the summer maximum growth in depth is diminished and the variability is lower than in winter.

5.2. *Depth–time rescaling*

According to the former analysis, the cyclone life cycle is determined by the growth of depth, which is in accord with canonical central pressure deepening with respect to the environment. In a first, conceptual approximation the radii obtained in the present analysis might be considered constant. Thus the different stages of the cyclone life cycles are visualized from a schematic point of view in Figure 1.

The behaviour of the depths in the cyclone classes suggests a data collapse similar to that of Rudeva and Gulev (2007) for the life cycles of the radii. This requires that the ages and the depths are scaled appropriately. The classes c are defined as the sets of cyclones with the same total age $\hat{a}(c)$. Thus the ages are scaled according to

$$\tilde{a} = \frac{a}{\hat{a}(c)}. \tag{5}$$

In a similar way, the depths are scaled by the maximum depth $\hat{D}(c, a)$ attained during the life cycle in the class c:

$$\tilde{D} = \frac{D - D_{\min}}{\hat{D}(c, a) - D_{\min}}, \tag{6}$$

where $D_{\min}$ is the minimum depth reached during a life cycle. The maximum depths $\hat{D}(c, a)$ are estimated by a fit within class c; this value is not the absolute maximum reached in the class. Figure 10 presents the data $(\tilde{D}, \tilde{a})$ collapsed according to these transformations (Eqs (5) and (6)) for winter and summer in ERA-40. Due to the definition in Eq. (6), the maximum of the scaled depths can be more than unity, whereas the scaled depths reach a minimum near zero (cyclogenesis) or maximum age (lysis). Cyclones with a maximum age of more than 8 days are excluded, since their number is too low (20) for the whole ERA-40 period.

The rescaled life cycles of the depths are compared with a simple parabola, $\propto \tilde{a}(1 - \tilde{a})$, which agrees well with the data, mainly in summer. Obviously, the weak cyclones follow this simple dynamic behaviour with a symmetry between growth and decay. Deviations from the symmetric behaviour are based on intense winter cyclones with large total age and a rapid growth during the first three days. This result agrees with the analysis of the rescaled effective radius of Rudeva and Gulev (2007), which is related to the Gaussian depths according to Figure 1 (when identified with R_{env}).

The data collapse presents a remarkable property of midlatitude cyclones. This result, which is denoted 'universal' by Rudeva and Gulev (2007), suggests that the principal dynamic behaviour of the vortices does not depend on the Gaussian radii: the dynamics is scaling and self-similar in time. Scaling is well-known in turbulence theory in both two and three dimensions, where statistical properties of Eulerian correlation functions follow power laws. The new aspect is that the time evolution initiated by baroclinic

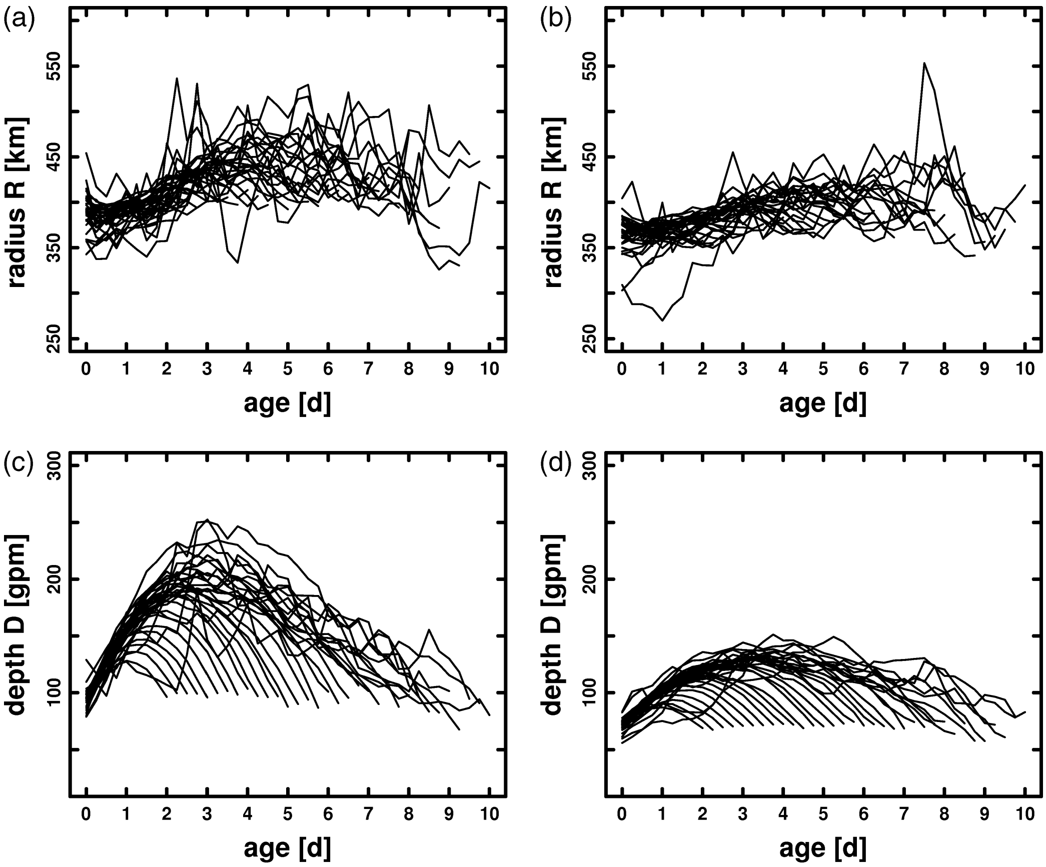

Figure 9. Evolution of (a,b) radii and (c,d) depths composited with respect to the total lifetime for winter (left) and summer (right).

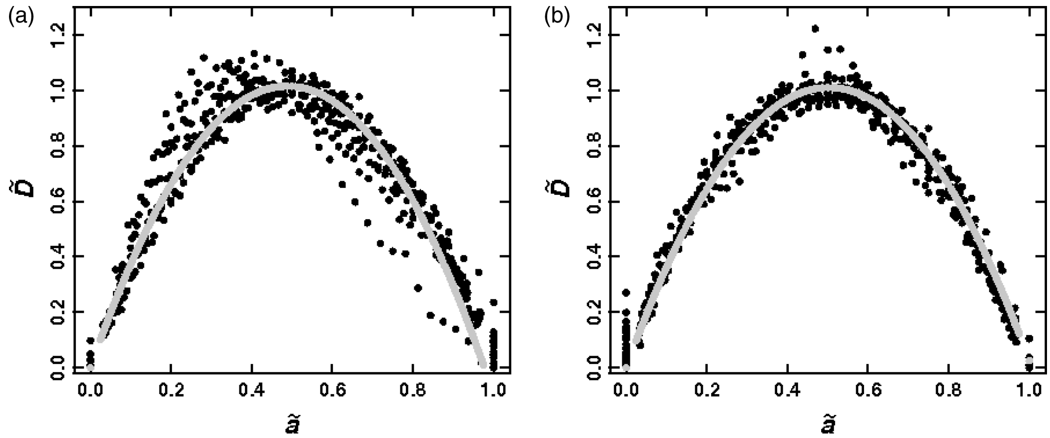

Figure 10. Rescaled depths versus rescaled age, for (a) winter and (b) summer (black dots) and a fitted parabola (grey).

dynamics is itself scaling in the Lagrangian perspective. The geostrophic vorticity can be scaled due to (4). Note that the geostrophic kinetic energy of a vortex at 1000 hPa height is proportional to D^2. Due to this relation, the life cycles of the geostrophic kinetic energy can be rescaled similarly to the depth.

6. Summary and discussion

Fitting an azimuthally symmetric Gaussian function to the 1000 hPa geopotential height of located cyclone centres and their surroundings provides a geometric analysis of midlatitude cyclones, thereby extending the analysis of Blender *et al.* (1997), which was confined to cyclone detection and their respective statistics. The adjusted Gaussian function yields two cyclonic parameters, radius (standard deviation) and depth, which is determined by the pressure deficit between the cyclone centre and a synoptic neighbourhood. To analyse cyclone life cycles, the trajectories are determined by a nearest neighbour search. The cyclones are detected in the ECMWF reanalysis ERA-40 data and in IPCC simulations with the coupled atmosphere–ocean model ECHAM5/MPI-OM for the present day and warmer climate scenario A1B. The analysis is applied to Northern Hemisphere winters and summers.

The obtained radii vary between 300 and 500 km in winter and 300–400 km in the summer season. In the present model, the radii show weak growth during the life cycles. The depths reveal intense deepening during the cyclone life cycles, lasting between 2 and 10 days. Since the radius defined in the Gaussian model equals the position of maximum wind speed, the present results coincide with the values of 450–650 km derived by Grotjahn and Castello (2000) for the maximum of the kinetic energy. The majority of the previously published cyclone size definitions, which are mostly based on the edge of the depressions, show values reaching more than 1000 km and pronounced growth during the life cycles. This discrepancy is explained within the current model, where the edge is located far beyond the radius and where the growth of the depth is responsible for the widening effect detectable at the edge of the depressions. Thus, this investigation confirms Grotjahn *et al.* (1999): 'many linear studies assume that cyclones do not change in size as they evolve'.

The Gaussian model yields geostrophically approximated wind and vorticity and thus yields direct relationships between geometry and dynamics. The vorticity is validated by a comparison with the simulated 850 hPa relative vorticity.

To determine the resolution dependence of the Gaussian model fit, the ERA-40 reanalysis data are mapped to $T42$, $T63$ and $T106$ spectral resolutions ($\approx 2.8°, 1.9°, 1.1°$). Note that the ECHAM5/MPI-OM IPCC scenario simulation is based on $T63$ resolution. The higher resolutions yield (1) a shift to smaller radii during winter and summer and (2) an increase of the number of shallow and weak cyclones, mainly during summer.

The cyclone densities in the 20C simulation with the ECHAM5/MPI-OM are validated by comparison with the ERA-40 reanalysis data for the winter and summer seasons. Deviations from the reanalysis are most pronounced in the summer season. In the warmer climate a distinct northward displacement of the cylone tracks is visible over the Northern Pacific during winter. This northward displacement is less distinctive in the North Atlantic region. In summer, the North Pacific cyclone density shows a pronounced southward shift, opposite to the North Atlantic region. The most noticeable change is predicted for the Mediterranean, with an increase of the cyclone density during summer and a decrease during winter.

The smallest radii are found in the genesis regions of the oceanic storm tracks, with similar values during winter and summer. The largest radii occur during winter in the lysis regions and over land. Pronounced depth maxima are located near the centres of the cyclone tracks, and the lowest depths are found in the cyclone genesis regions and over land. The seasonal cycle of the depths is much more intense than that of the radii. Thus radii and depths reveal no coherent behaviour.

The cyclone radii in the 20C simulation agree with the reanalysis during winter, while the radii are slightly enhanced during summer. The frequency distribution of the depths shows a slight underestimation of shallow cyclones and weak overestimation of deep systems in 20C for winter and summer, pointing to an underestimation of small-scale synoptic systems. This insufficient representation of small-scale cyclones is due to the lower resolution of the climate model.

In the warmer climate, simulated in the A1B scenario, the frequency of the smallest radii increases in summer. The frequency distribution reveals a slight increase for deep cyclones for winter and summer. Both radius and depth frequency distributions indicate a shift of the geometric properties in the A1B scenario.

The geographical distributions of radii and depth hint at relationships with the cyclone life cycles. The radii reveal weak growth during the life cycles, with distinctly larger values in winter compared with summer. The depths, however, show pronounced life cycles in winter and summer. It is possible to collapse the depth life cycles if the depths and the ages are scaled by maximum values (see Rudeva and Gulev (2007) for a similar analysis of the radius life cycles). The rescaled depth life cycles can be described by a simple universal function, $\tilde{a}(1-\tilde{a})$, with $\tilde{a}$ being the relative age of the cyclone. This function yields a surprisingly simple representation of the cyclone life cycles during summer. The deviation from this function during winter is mainly caused by cyclones with a total age higher than six days.

The present Gaussian model for the geometric structure of midlatitude depressions yields a concise dynamic aspect of the cyclone life cycles. The new result is that the radii, if defined as a decay scale, reveal weak growth during the life cycles and attain values between 300 and 500 km. The data are hardly distinguishable by their total lifetimes and the radii are constrained to a narrow band of not more than 100 km width. On the other hand, the life cycles of the depths (or pressure deficits) are well represented by a universal function, which is mainly valid for weak cyclones. Thus, the growth of the radii is determined by a different mechanism than that of the depths. Furthermore, the rescaled depths show that growth and decay are symmetric and distinctly different from exponential behaviour.

In high-resolution analyses from the ECMWF, Jung *et al.* (2006) find cyclones at all scales down to approximately 20 km, limited by the given spectral truncation $T512$ of the analyses. Obviously, midlatitude cyclones are produced not only by baroclinic instability but also by nonlinear cascade processes, suggesting that synoptic cyclones exist at all spatial scales and that the concept of a mean vortex size may be not meaningful. That is, the result for the mean may depend substantially on the resolution of data (Jung *et al.*, 2006).

Therefore, the derivation of a cyclone radius in gridded data leads to numerical difficulties, since the present-day data set resolutions are not sufficient for a detailed description of all synoptic disturbances. This means that all methods that consider grid-point values in the neighbourhood of a pressure minimum do not find smooth pressure (or geopotential height) fields where notions like radial lines, saddle points, or even closed isobars can be realized with sufficient accuracy. Problems with gridded data are avoided by integral approaches as in Grotjahn *et al.* (1999) and Benestad and Chen (2006).

The concept of a cyclone radius assumes azimuthal symmetry. This point of view reveals several advantages, since any deviation from azimuthal symmetry leads to additional characteristics, which are difficult to compare with other analyses (note that even the presently used definitions for the radius are hardly comparable). Furthermore, the finite resolution of gridded data sets and the presence of vortices at all spatial scales hinders the calculation of detailed geometric properties.

Acknowledgements

We thank the anonymous reviewers for helpful comments. Discussions with Oliver Bothe, Kerstin Haberkorn, Frank Lunkeit, Kathrin Riemann-Campe and Frank Sienz are acknowledged. Financial support was provided by the

Deutsche Forschungsgemeinschaft (SFB-512). The data are provided by the CERA data base Hamburg (http://cera-www.dkrz.de/WDCC/ui/Index.jsp). The R Development Core Team is acknowledged for the statistical package R.

References

Benestad RE, Chen D. 2006. The use of a calculus-based cyclone identification method for generating storm statistics. *Tellus A* **58**: 473–486.

Bengtsson L, Hodges KI, Roeckner E. 2006. Storm tracks and climate change. *J. Climate* **19**: 3518–3543.

Blender R, Fraedrich K, Lunkeit F. 1997. Identification of cyclone-track regimes in the North Atlantic. *Q. J. R. Meteorol. Soc.* **123**: 727–741.

Blender R, Schubert M. 2000. Cyclone tracking in different spatial and temporal resolutions. *Mon. Weather Rev.* **128**: 377–384.

Grigoriev S, Gulev SK, Zolina O. 2000. Innovative software facilities cyclone tracking and analysis. *Eos, Trans. Amer. Geophys. Union* **81**: 170.

Grotjahn R, Castello C. 2000. A study of frontal cyclone surface and 300-hPa geostrophic kinetic energy distribution and scale change. *Mon. Weather. Rev.* **128**: 2865–2874.

Grotjahn R, Hodyss D, Castello C. 1999. Do frontal cyclones change size? Observed widths of North Pacific lows. *Mon. Weather Rev.* **127**: 1089–1095.

Hodges KI. 1994. A general method for tracking analysis and its application to meteorological data. *Mon. Weather Rev.* **122**: 2573–2586.

Jiang J, Perrie W. 2007. The impacts of climate change on autumn North Atlantic midlatitude cyclones. *J. Climate.* **20**: 1174–1187.

Jung T, Gulev SK, Rudeva I, Soloviov V. 2006. Sensitivity of extratropical cyclone characteristics to horizontal resolution in the ECMWF model. *Q. J. R. Meteorol. Soc.* **132**: 1839–1857.

Jungclaus JH, Keenlyside N, Botzet M, Kaak H, Luo J-J, Latif M, Marotzke J, Mikolajewicz U, Roeckner E. 2006. Ocean circulation and tropical variability in the coupled model ECHAM5/MPI-OM. *J. Climate* **19**: 3952–3972.

König W, Sausen R, Sielmann F. 1993. Objective identification of cyclones in GCM simulations. *J. Climate* **6**: 2217–2213.

Lim E-P, Simmonds I. 2007. Southern Hemisphere winter extratropical cyclone characteristics and vertical organization observed with the ERA-40 reanalysis data in 1979-2001. *J. Climate* **20**: 2675–2690.

Löptien U, Zolina O, Gulev S, Latif M, Soloviov V. 2008. Cyclone life cycle characteristics over the Northern Hemisphere in coupled GCMs. *Clim. Dyn.* **31**: 507–532.

Marsland SJ, Haak H, Jungclaus JH, Latif M, Röske F. 2003. The Max-Planck-Institute global ocean/sea ice model with orthogonal curvilinear coordinates. *Ocean Modelling* **5**: 91–127.

Murray RJ, Simmonds I. 1991. A numerical scheme for tracking cyclone centres from digital data. Part I: development and operation of the scheme. *Aust. Meteorol. Mag.* **39**: 167–180.

Nakicenovic N, Alcamo J, Davis G, de Vries B, Fenhann J, Gaffin S, Gregory K, Grübler A, Jung TY, Kram T, La Rovere EL, Michaelis L, Mori S, Morita T, Pepper W, Pitcher HM, Price L, Riahi K, Roehrl A, Rogner HH, Sankovski A, Schlesinger M, Shukla P, Smith SJ, Swart R, van Rooijen S, Victor N, Dadi Z. 2000. *Special Report on Emissions Scenarios*. Cambridge University Press: Cambridge; 599pp.

Nielsen JW, Dole RM. 1992. A survey of extratropical cyclone characteristics during GALE. *Mon. Weather Rev.* **120**: 1156–1167.

Patoux J, Yuan X, Li C. 2009. Satellite-based midlatitude cyclone statistics over the Southern Ocean: 1. Scatterometer-derived pressure fields and storm tracking. *J. Geophys. Res.* **114**: D04105. DOI:10.1029/2008JD010873.

Pinto JG, Ulbrich U, Leckebusch GC, Spangehl T, Reyers M, Zacharias S. 2007. Changes in storm track and cyclone activity in three SRES ensemble experiments with the ECHAM5/MPI-OM1 GCM. *Clim. Dyn.* **29**: 195–210.

Pinto JG, Zacharias S, Fink AH, Leckebusch GC, Ulbrich U. 2009. Factors contributing to the development of extreme North Atlantic cyclones and their relation with the NAO. *Clim. Dyn.* **32**: 711–737.

R Development Core Team. 2007. *R: A language and environment for statistical computing.* R Foundation for Statistical Computing: Vienna, Austria; ISBN 3-900051-07-0. URL: http://www.R-project.org.

Roeckner E, Bäuml G, Bonaventura L, Brokopf R, Esch M, Giorgetta M, Hagemann S, Kirchner I, Kornblueh L, Manzini E, Rhodin A, Schlese U, Schulzweida U, Tompkins A. 2003. '*The atmospheric general circulation model ECHAM5, part I: Model description*', MPI Rep. 349, 127pp.

Rudeva IA. 2008. On the relation of the number of extratropical cyclones to their sizes. *Izvestiya Atmospheric and Oceanic Physics* **44**: 273–278.

Rudeva IA, Gulev SK. 2007. Climatology of cyclone size characteristics and their changes during the cyclone life cycle. *Mon. Weather Rev.* **135**: 2568–2587.

Schubert M, Perlwitz J, Blender R, Fraedrich K. 1998. North Atlantic cyclones in CO_2-induced warm climate simulations: frequency, intensity, and tracks. *Clim. Dyn.* **14**: 827–837.

Sickmöller M, Blender R, Fraedrich K. 2000. Observed winter cyclone tracks in the Northern Hemisphere in reanalysed ECMWF data. *Q. J. R. Meteorol. Soc.* **126**: 591–620.

Simmonds I. 2000. Size changes over the life of sea level cyclones in the NCEP reanalysis. *Mon. Weather Rev.* **128**: 4118–4125.

Simmonds I, Keay K. 2000. Variability of southern hemisphere extratropical cyclone behaviour, 1958–97. *J. Climate* **13**: 550–561.

Simmonds I, Keay K. 2002. Surface fluxes of momentum and mechanical energy over the North Pacific and North Atlantic Oceans. *Meteorol. Atmos. Phys.* **80**: 1–18.

Simmons AJ. 2001. Development of the ERA-40 data assimilation system. *ERA-40 Project Report Ser.* **3**: 11–30.

Sinclair MR. 1994. An objective cyclone climatology for the Southern Hemisphere. *Mon. Weather Rev.* **122**: 2239–2256.

Trigo IF, Davies TD, Bigg GR. 1999. Objective climatology of cyclones in the Mediterranean region. *J. Climate* **12**: 1685–1696.

Ulbrich U, Leckebusch GC, Pinto JG. 2009. Extra-tropical cyclones in the present and future climate: a review. *Theor. Appl. Climatol.* **96**: 117–131.

Uppala SM, Kållberg PW, Simmons AJ, Andrae U, Da Costa Bechtold V, Fiorino M, Gibson JK, Haseler J, Hernandez A, Kelly GA, Li X, Onogi K, Saarinen S, Sokka N, Allan RP, Andersson E, Arpe K, Balmaseda MA, Beljaars ACM, van de Berg L, Bidlot J, Bormann N, Caires S, Chevallier F, Dethof A, Dragosavac M, Fisher M, Fuentes M, Hagemann S, Hólm E, Hoskins BJ, Isaksen L, Janssen PAEM, Jenne R, McNally AP, Mahfouf J-F, Morcrette J-J, Rayner NA, Saunders RW, Simon P, Sterl A, Trenberth KE, Untch A, Vasiljevic D, Viterbo P, Woollen J. 2005. The ERA-40 reanalysis. *Q. J. R. Meteorol. Soc.* **131**: 2961–3012.

Wernli H, Schwierz C. 2006. Surface cyclones in the ERA-40 dataset (1958-2001). Part I: Novel identification method and global climatology. *J. Atmos. Sci.* **63**: 2486–2507.

